J Solid State Electrochem (2006) 10: 320–328
DOI 10.1007/s10008-005-0094-7

ORIGINAL PAPER

Marina V. Makarova · Kateřina Macounová · Petr Krtil

The effect of cationic disorder on the optical and electrochemical behavior of nanocrystalline ZnO prepared from peroxide precursors

Received: 20 July 2005 / Revised: 7 August 2005 / Accepted: 14 December 2005 / Published online: 22 February 2006

Abstract The relation between particle size and the optical and electrochemical behavior of nanocrystalline ZnO was studied on materials prepared by the thermal decomposition of zinc peroxide. The formation of zinc oxide starts at 180°C and yields particles of characteristic size bigger than 10 nm. Smaller particles (r~2–5 nm) may be prepared at reduced pressure and at a temperature of 150°C. The particle radius of synthesized nanocrystals increases proportionally to synthesis temperature. Regardless of actual particle size, synthesized ZnO samples show cationic disorder, with Zn distributed between 2*b* and 2*a* sites. The fraction of "octahedrally" coordinated Zn in 2*a* position decreases with increasing synthesis temperature. Zn disorder causes a narrowing of band gap, which results in the "red shift" of the absorption edge in the UV–Vis spectra of prepared samples with respect to bulk ZnO. The effect of the disorder on the band gap width is partially compensated by quantum size effects when the characteristic particle size drops below 5 nm. A decrease in particle size results in an asymmetric shift of valence and conduction band edges, which can be assigned to uneven effective masses of electrons and holes in nanocrystalline ZnO. Prepared nanocrystalline samples were (photo)electrochemically active; their activity, however, decreases with particle size.

Keywords Coherent domain · Zinc oxide · (Photo)electrochemistry · Quantum size effects

M. V. Makarova · K. Macounová · P. Krtil (✉)
J. Heyrovsky Institute of Physical Chemistry,
Academy of Sciences of the Czech Republic,
Dolejskova 3,
18223 Prague, Czech Republic
e-mail: Petr.Krtil@jh-inst.cas.cz
Tel.: +420-266053826
Fax: +420-286582307

Introduction

Wide band gap semiconductor oxides are prospective materials for various practical applications, such as (photo) electrochemical solar cells [1], chemical sensors [2, 3], UV lasers [4, 5], or single-electron electronics [6, 7]. Nanocrystalline forms of these oxides are particularly interesting, since they allow the preparation of devices with electrodes of high specific surface area and good control of interfacial properties [1]. In addition, one may expect nanocrystalline semiconductor oxides to show a behavior significantly different from that of bulk materials when the characteristic particle size of the material becomes comparable with that of the mean size of excitons in the material [8]. These so-called quantum size effects manifest themselves by broadening band gap and by shifting both valence and conduction band edges toward more negative and positive energies, respectively [1b].

ZnO belongs, along with TiO_2, to the most popular oxide n-semiconductors [1b, 9–11]. It has a band gap energy of 3.2 eV (at 300 K) [12] and is primarily considered as a material for UV photoelectric devices. Nanocrystalline ZnO materials of dimensions comparable with those showing quantum effects can be prepared by thermophysical, mechanochemical, and chemical methods [8, 13–17]. Chemical routes use a precipitation scheme, i.e., direct precipitation [13–17] or the thermal decomposition of an intermediate precursor. Such precursors can be zinc oxalate [18], hydroxycarbonate [13], alcoxide [8], hydroxide [14], acetate [15], sulfide [16], or peroxide [17]. These reactions proceed at temperatures in the range of 250–600°C, depending on precursor type. The resulting particles fall in the region of 2–100 nm [8, 14–16, 18]. Despite the fact that characteristic particle sizes of prepared materials often fall within the region where quantum size effects should apply, the actual behavior of synthesized nanocrystals may be significantly different. For instance, nanocrystalline ZnO prepared from peroxide precursors is reported to show a narrower band gap with respect to bulk ZnO [17, 18]. The origin of this band gap narrowing and its consequences to

the (photo)electrochemical behavior of the resulting zinc oxide are not yet understood.

This work focuses on a systematic study of particle size effects in the case of nanocrystalline ZnO prepared from peroxide precursors. The scope of the synthetic approach is extended by the addition of reaction pressure control. The relationship between synthetic conditions, the actual crystalline structure of nanoparticles, and the resulting electronic structure is based on X-ray diffraction (XRD), transmission electron microscopy (TEM), UV–Vis spectroscopy, and electrochemical data. The consequences of the actual electronic structure resulting from nanocrystalline ZnO electrodes are discussed.

Experimental

Microcrystalline ZnO powder (Lachema, p.a.) was stoichiometrically dissolved in nitric acid (Lachema, p.a.) to obtain a 2M Zn^{2+} solution. The neutral Zn^{2+} solution was slowly added to the mixture of 35% H_2O_2 and ammonia (1:2 molar ratio; both from Fluka, p.a.). The total amount of added zinc solution was set to obtain a reaction mixture characterized by a 1:2:4 molar ratio of zinc, peroxide, and ammonia, respectively. The reaction mixture was intensively cooled during reaction using an ice bath. A white precipitate of zinc peroxide that formed in the reaction was filtered out, washed thoroughly with deionized water to remove an excess of ammonia and hydrogen peroxide, and air-dried at room temperature. Peroxide precursors were subsequently decomposed at temperatures ranging between 150 and 400°C at atmospheric or reduced pressure. The processing conditions are summarized in Table 1. The resulting materials were of white or light-yellow color.

The structural characterization of synthesized peroxide precursors and of final nanocrystalline ZnO samples was based on powder XRD performed using Siemens D8 Advanced Powder X-ray Diffractometer with Vantage1 detector and CuKα radiation. Measured diffractograms were refined by Rietveld analysis using Powdercell Software. Characteristic particle/coherent domain size data were obtained by the Warren–Averbach method using the WINFIT program for peak profile analysis [19]. Information on the particle size/shape of the prepared ZnO nanocrystals was gathered from transmission electron micrographs recorded using a Philips EM 201 transmission electron microscope. The materials with the smallest particle size were characterized also by high-resolution transmission electron microscopy (HRTEM) using a Jeol 3010 microscope. Information on particle size distribution was obtained by analyses of TEM and HRTEM micrographs, taking into account 70–150 randomly selected particles. The thermal behavior of the prepared samples was studied using a Netzsch STA 409 differential thermal analysis (DTA)/thermogravimetric analysis apparatus. Thermogravimetry (TG)/DTA data were acquired on air in the interval 20–350°C at a heating rate of 2°C/min.

Optical properties of synthesized ZnO samples were studied by UV–Vis–NIR spectroscopy in diffuse reflection measurements using a Perkin-Elmer UV–Vis–NIR Lambda 19 spectrometer. UV–Vis–NIR spectra were measured in a quartz cuvette (2 mm thick) in a spectral range of 200–2,500 nm. The original reflectance data were recalculated using the Kubelka–Munk theory.

The electrochemical behavior of nanocrystalline ZnO materials was tested on thin film electrodes prepared by a spin coating procedure [9]. The thin films of nanocrystalline ZnO samples were prepared from zinc oxide suspensions in absolute ethanol (ZnO concentration 0.02 g/ml). Fifty microliters of suspension was placed on the surface of F^--doped SnO_2 electrodes [20], and the electrode was spun at 800 rpm for 1 min to remove an excess of ethanol. The prepared layer was stabilized by heating at 100°C (70°C for material with coherent domain size below 4 nm) for 5 min. The spin coating procedure was repeated ten times to obtain electrodes with sufficient surface coverage. After the deposition of the last layer, the whole film electrode was stabilized by annealing at 320°C for 30 min to improve the mechanical stability of the electrodes.

All electrochemical and (photo)electrochemical experiments were carried out in a single-compartment cell and a three-electrode arrangement with ZnO working electrode, Pt auxiliary electrode, and Ag/AgCl reference electrode. The potential in (photo)electrochemical experiments was controlled using a PAR 263 A potentiostat. Mott–Schottky plots were constructed from AC impedance data measured at a frequency of 6 Hz, with an AC amplitude of 10 mV (rms). AC measurements were carried out using a Solartron 1286 electrochemical interface, combined with a Solartron 1250 analyzer. A xenon lamp (400 W; Applied Photophysics) was used as a polychromatic illumination source in (photo)electrochemical experiments.

Table 1 Crystallographic properties of ZnO samples prepared from peroxide precursors

t_{ann} (°C)	Time (h)	P (kPa)	Zn^{2+} site occupancy			Lattice constants (Å)	
			2*a*	2*b*	[Zn]:[O]	*a*	*c*
150	3	1	0.10	0.85	0.88	3.25	5.23
200	1	1	0.09	0.89	0.92	3.25	5.23
180	2	100	0.08	0.88	0.91	3.25	5.23
300	2	100	0.03	0.93	0.94	3.25	5.21
400	4	100	0.02	0.94	0.95	3.25	5.21

Results and discussion

Structure of precursor and final products

The XRD data show that the precipitation of Zn^{2+} by peroxide in ammonium bath leads to the formation of a crystalline product (curve *a*) in Fig. 1). The diffraction pattern of the precursor agrees well with that corresponding to single-phase ZnO_2 [21]. The experimentally recorded diffraction pattern can be indexed assuming a cubic

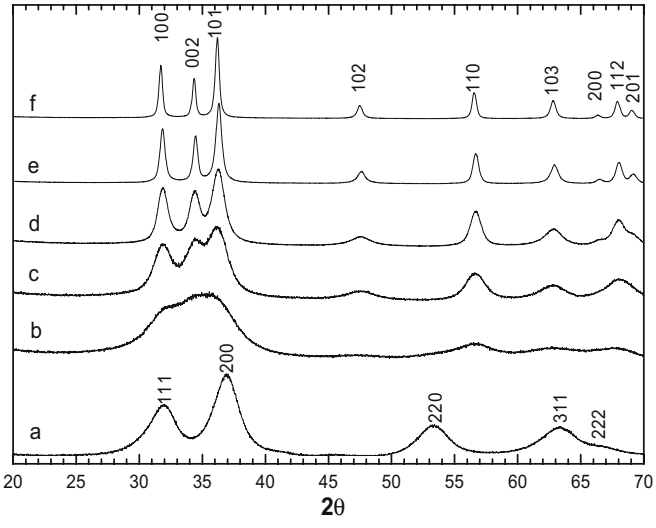

Fig. 1 XRD spectra of samples annealed at different temperatures in air and in vacuum: *a* initial ZnO_2; *b* 150°C at 1 kPa; *c* 200°C at 1 kPa; *d* 180°C at 101 kPa; *e* 300°C at 101 kPa; *f* 400°C at 101 kPa

structure (*Pa-3*) with a lattice constant a=4.88 Å. Zinc peroxide precursors are sufficiently stable at temperatures below 150°C. TG/DTA measurements indicate a mass decrease of ca. 3% in this temperature interval (Fig. 2), which may be attributed to loss of adsorbed water. When the temperature exceeds 180°C, one observes a rapid mass decrease, which results from an exothermic process. The total mass decrease triggered by this exothermic process is about 16% and may be attributed to zinc peroxide decomposition proceeding according to the following stoichiometry:

$$ZnO_2 \rightarrow ZnO + 0.5O_2 \uparrow. \quad (1)$$

Note that the observed temperature of peroxide decomposition is ca. 50°C lower than that reported in the literature [17]. The temperature of peroxide decomposition may be further decreased by reducing pressure during the annealing process. At pressures corresponding to ca. 1 kPa, we observe zinc oxide formation at temperatures as low as ~150°C. Zinc peroxide decomposition reflects itself also in measured diffraction patterns (Fig. 1). The diffraction patterns recorded on materials annealed at 180°C (150°C at reduced pressure) and higher show only the peaks that may be attributed to a hexagonal structure of wurtzite type ($P_{63}mc$). The crystallinity of the ZnO samples improves with increasing annealing temperature; the annealing time has a minor effect on the quality of the diffraction patterns. According to XRD data, the reaction at lowered pressure leads to the formation of materials with finer crystals.

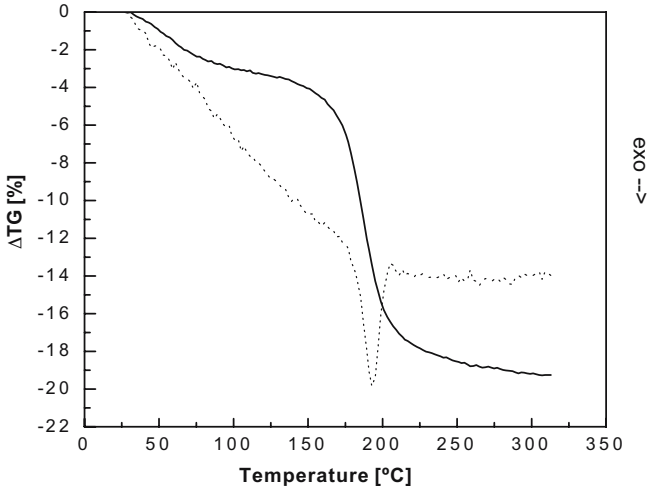

Fig. 2 TG (*solid line*) and DTA (*dotted line*) curves of ZnO_2 decomposition. Heating rate, 2°C/min

Measured diffraction patterns were analyzed using Rietveld refinement to obtain information on both lattice parameters and disorder within the structure. The lattice constants found in all samples seemed to be little affected by the annealing temperature and were found to be a=3.250±0.005 Å and c=5.210±0.005 Å. These values are in good agreement with literature data [22]. Experimental diffraction patterns show, however, a slight deviation of relative intensities (particularly for reflection <*102*>) with respect to database standard. Such a behavior indicates presence of disorder either in oxygen or zinc sublattice. The results of the Rietveld refinement (which are summarized in Table 1) clearly show that a satisfactory fit of experimental diffraction patterns cannot be obtained unless one assumes a disorder of zinc between 2*a* and 2*b* sites (in Wykoff notation) of the expected wurtzite structure. While the 2*b* site (the only one occupied in standard ZnO) represents zinc in tetrahedral coordination, the 2*a* site represents zinc coordinated by a distorted bipyramid. With respect to different coordination numbers of zinc in both 2*a* and 2*b* positions (the multiplicity of zinc in 2*a* position is three times smaller than that of zinc in 2*b* position), we have to expect a slight excess of oxygen with respect to zinc oxide stoichiometry (Table 1). To satisfy electroneutrality condition, one has to assume that this "overstoichiometric" oxygen is of a higher oxidation state than −II. Keeping in mind that the zinc oxide was formed from zinc peroxide (which had octahedral coordination of zinc), we might attribute the zinc in 2*a* positions to a transition between peroxide and oxide structures, which remained kinetically frozen in prepared materials. Note that the results of Rietveld analysis contradicted those of Uekawa et al. [17], who used the titration technique to propose oxygen deficiency for ZnO samples made from peroxide precursors.

Particle size analysis

Zinc peroxide decomposition leads to the formation of rather fine oxide particles. As shown in the TEM data (Fig. 3), the materials annealed in air have spherical particles with a characteristic particle diameter of 3–50 nm, depending on the annealing temperature (Fig. 3a–c). The spherical particle shape converts eventually (at a temperature of 400°C) into hexagonally shaped crystals. In

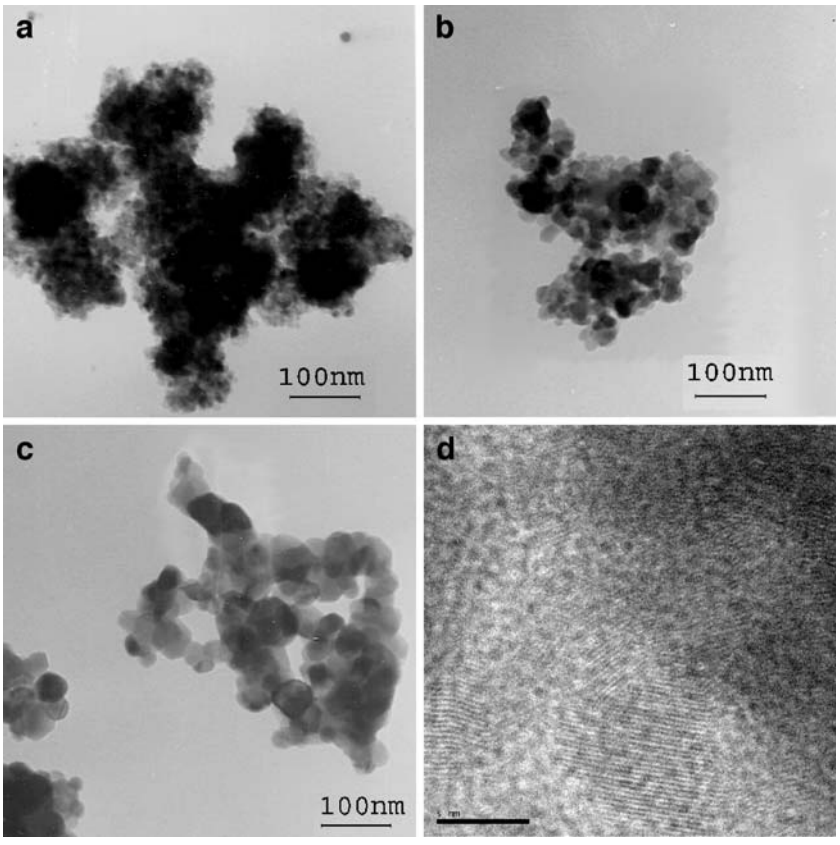

Fig. 3 TEM images of ZnO samples prepared at different temperatures and pressures: **a** 180°C at 101 kPa; **b** 300°C at 101 kPa; **c** 400°C at 101 kPa; **d** 150°C at 1 kPa (HRTEM image)

contrast to that the materials growing at reduced pressure form much smaller crystallites (3–5 nm), which form aggregates of ~50–100 nm in size. As shown in Fig. 3d, the crystallites prepared at reduced pressure are embedded in a small amount of amorphous matrix. Particle size and distribution width increase with the synthetic temperature (Figs. 4 and 5; Table 2).

Particle size data extracted from TEM measurements do not agree with characteristic length parameter, which can be obtained by analyses of diffraction line widths

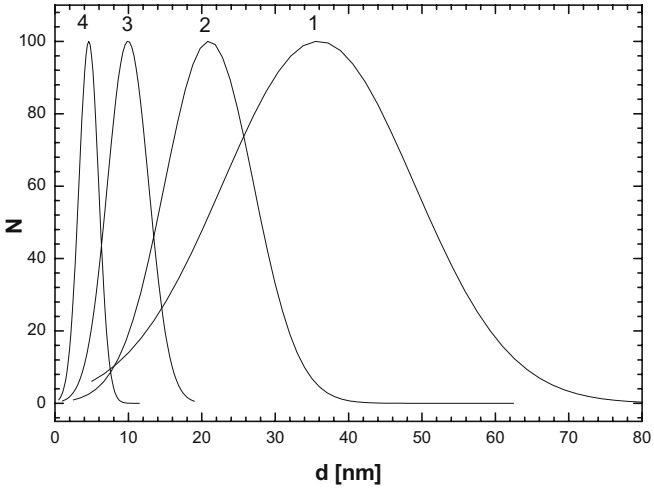

Fig. 4 Particle size distribution curves extracted from analyses of TEM micrographs of ZnO samples prepared at different temperatures and pressures: *1* 400°C at 101 kPa; *2* 300°C at 101 kPa; *3* 180°C at 101 kPa; *4* 150°C at 1 kPa

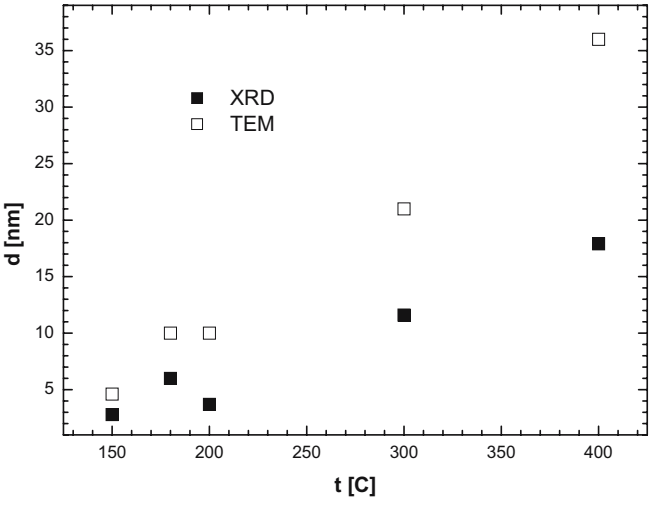

Fig. 5 Particle size estimated from TEM and XRD measurements as a function of synthetic temperature

Table 2 Particles and coherent domain size depending on temperature for samples prepared in air and in vacuum

t_{ann} (°C)	P (kPa)	Coherent domain size (nm)			Particle size (TEM; nm)
		D_F	D_I	$D=(D_I+D_F)/2$	
180	100	5.2±0.7	6.7±0.8	6.0	10±3
300	100	9.5±1.4	13.6±2	11.6	21±6
400	100	14.6±3	21.2±2.6	17.9	36±13
150	1	2.8±0.3	2.8±0.6	2.8	4.6±1.4
200	1	3.4±0.3	3.9±0.4	3.7	–

[24]. This discrepancy is usually attributed to the presence of smaller coherent domains tilted by a small angle (<5°), which causes broadening of experimental diffraction lines. Coherent domain sizes are obtained by Fourier analysis of diffraction peaks corresponding to *<100>*, *<002>*, *<101>*, *<110>*, *<102>*, and *<103>* directions. The effective domain size D_F is calculated from the initial slope of Fourier coefficients. The integral value D_I is calculated by summarization of all Fourier coefficients, giving the mean square domain size [23]. The coherent domain sizes are listed in Table 2. The coherent domain size grows with increasing annealing temperature. Comparing the particle size found in TEM with the coherent domain size, it can be concluded that each particle contains from one to eight coherent domains. Some of the coherent domains may be demonstrated in HRTEM images (Fig. 3d); the small-angled character of boundaries between coherent domains prevents their direct observation in most cases.

Optical and electrochemical properties

The UV–Vis–NIR spectra of prepared materials are shown in Fig. 6. The edge of continuous absorption shows variations with the observed particle size as it shifts from ca. 3.25 to 3.3 eV. As can be seen in Fig. 6, the absorption edge of materials prepared at atmospheric pressure is red-shifted with respect to standard bulk ZnO. The materials prepared at reduced pressure show, on the other hand, a blue shift of the absorption spectrum edge. The variability of the absorption edge can be explained keeping in mind the fact that ZnO is the n-semiconductor, the band gap of which depends on the size of the nanoparticle. The decrease of the nanoparticle size causes broadening of the band gap of the material, which results in a shift of the absorption edge to shorter wavelengths (higher energies) with decreasing particle size. The theory predicts that this effect will occur when the particle radius becomes comparable or smaller than that of the Bohr exciton. An effective radius of Bohr exciton can be expressed [24]:

$$r_B = \frac{\hbar^2 \varepsilon m_0}{e^2 \mu} \tag{2}$$

where $\hbar$ is the Planck constant divided by 2π, ε is the dielectric constant, e is the electron charge, and μ is the effective exciton mass $\mu = m_e m_h/(m_e+m_h)$, where m_h and m_e are masses of hole and electron, respectively. In the case of ZnO, one may expect r_B to range between 0.9 and 2 nm, depending on the type of electron and hole subbands [25–

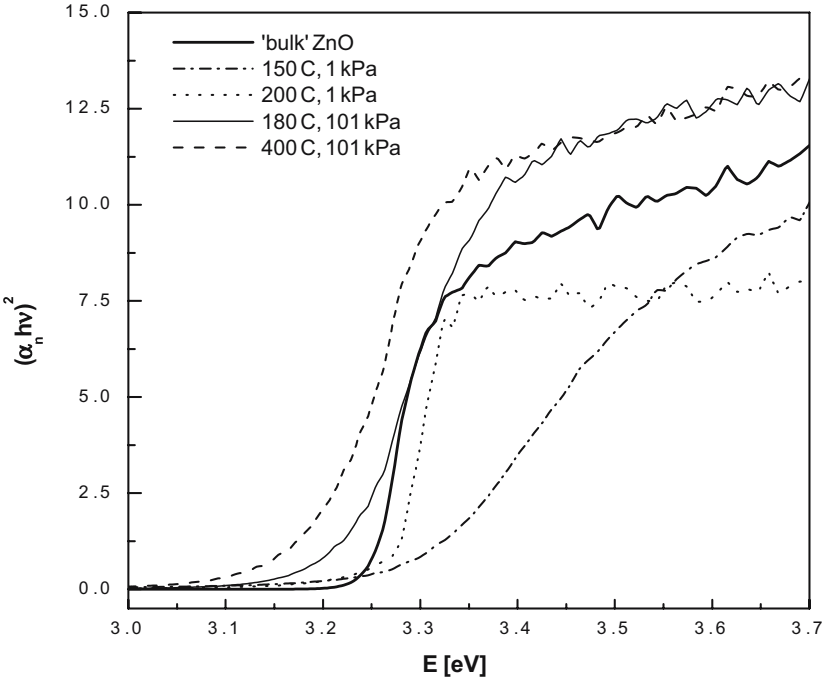

Fig. 6 UV–Vis spectra of the nanocrystalline ZnO samples prepared at different temperatures and pressures. The sample assignment is given in the figure legend

27]. These so-called quantum size effects are, in the case of ZnO, considered to take effect in particles up to three times larger than the exciton size [27] (i.e., in particles below 6–12 nm in diameter). These quantum size effects are predicted to cause effective broadening of semiconductors' band gaps according to the formula [26, 28]:

$$E^* = E_g + \frac{h^2}{8\mu R^2} - \frac{1.8e^2}{4\pi\varepsilon_0\varepsilon_\infty R} \quad (3)$$

where E_g is the band gap in bulk material, ε is the dielectric constant of vacuum, and R is the particle radius. In the case of ZnO, we may convert the formula into the following form [29]:

$$E^* = E_g + \frac{2.1}{R^2} - \frac{0.297}{R} \quad (4)$$

It ought to be stressed that the red shift of the absorption edge observed in our experiments is not compatible with the above outlined theory. In addition, the quantitative comparison of the band gap broadening observed for samples prepared at lowered pressure is smaller than that predicted by the theory (Fig. 7). A similar "red shift" of the absorption edge with respect to bulk material was observed previously and was related to shallow and deep energy levels within the band gap [17, 30]. Although the experimentally observed band gap energies of our samples do not conform to the above outlined theory, their size dependence can be described by the same type of function as given in Eq. 3 (Fig. 7). The systematic deviation of experimental data from the theoretical ones then can be assigned to the disorder of ZnO structure.

The band structure of nanocrystalline ZnO in turn affects its electrochemical behavior, since the flat band potential (E_{fb}) is energetically identical to the lower edge of the conduction band. The information on flat band potential may be gathered either by measuring Mott–Schottky dependence or by determining the potential of photocurrent onset. Typical Mott–Schottky plot and voltammetric curve from a photocurrent experiment are shown in Fig. 8a,b. Flat band potential values can be used in combination with experimental band gap energies to determine the upper edge of the valence band in ZnO. The flat band potential values (determined from Mott–Schottky dependence and by photocurrent measurements), along with energies of the band edges of prepared materials, are summarized in Table 3. The dependence of band edge energies on the characteristic particle size is graphically represented in Fig. 9. The trend observed for flat band position clearly outlines electrochemical response which may be expected for nanocrystalline samples of different particle sizes. In general, the ZnO prepared from peroxide precursors shows the transition between depletion regime and accumulation regime at a more positive potential than conventional bulk ZnO (note that the electrochemical potential scale has

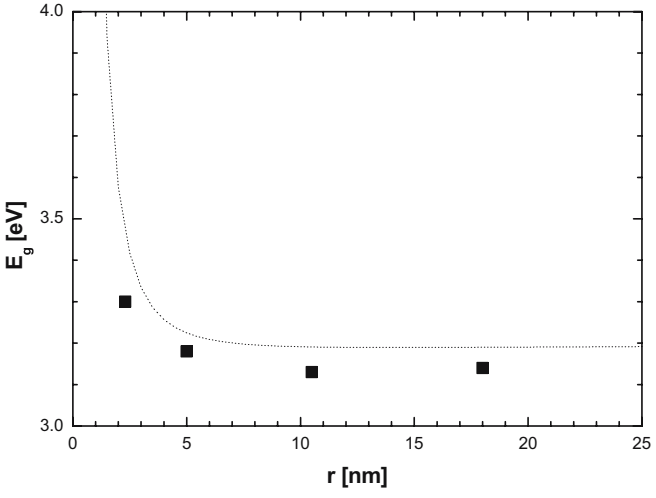

Fig. 7 Band gap energy (E_g) as a function of particle radius. The *dotted line* represents the theoretical prediction of E_g vs r dependence based on Eqs. 3 and 4

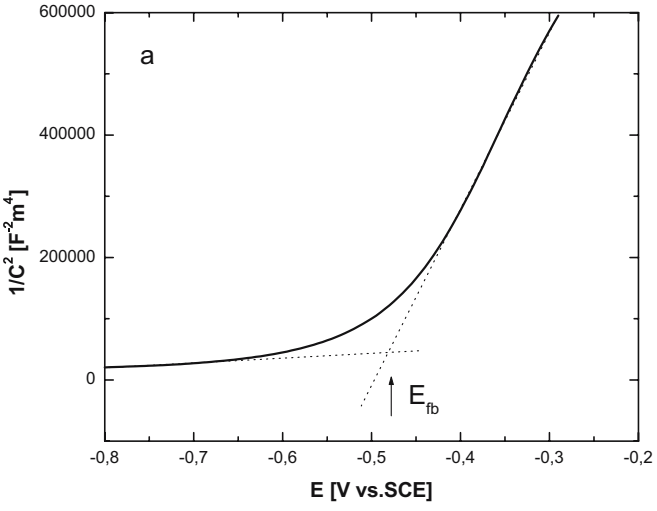

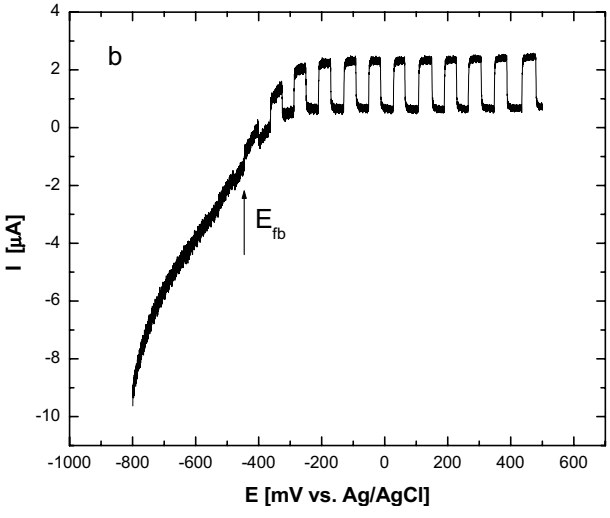

Fig. 8 **a** A typical Mott–Schottky plot for a ZnO nanocrystalline electrode. **b** A typical voltammetric curve of a nanocrystalline ZnO electrode under intermittent illumination. The data were measured on a material with a characteristic particle size of 40 nm

Table 3 Flat band potentials and band edge energies of nanocrystalline ZnO prepared from peroxide precursors

Particle size (nm)	E_{fb} vs NHE (mV)	E_g[a] (eV)	Potential of the lower edge of CB (eV)[b]	Potential of the upper edge of VB (eV)[b]	Photocurrent (%)
(A) E_{fb} values determined from photocurrent measurements (pH 7.0)					
4.6	–	3.30	–	–	0
6.0	−335	3.28	−4.165	−7.445	150
10.0	−143	3.22	−4.357	−7.577	700
21.0	−122	3.19	−4.378	−7.568	80
36.0	−162	3.2	−4.338	−7.538	180
>1,000	−286	3.25	−4.214	−7.464	150
(B) E_{fb} was determined from Mott–Schottky dependence (pH 8.6)					
4.6	−320	3.30	−4.180	−7.480	–
10.0	−228	3.19	−4.272	−7.462	–
21.0	−215	3.16	−4.285	−7.445	–
36.0	−221	3.18	−4.279	−7.459	–
>1,000	−388	3.25	−4.112	−7.362	–

[a]Data from UV–Vis spectra
[b]The potential values of conduction band (CB) and valence band (VB) edges are related to the vacuum level as a reference

orientation opposite to that of the energetic scale, expressed in absolute energies). This slightly disfavors these materials for possible application in, for example, solar cells. The inconvenience of the flat band potential position may be, on the other hand, compensated by a narrower band gap of these materials. A decrease of particle size leads to an improvement of the flat band position. This positive effect is, on the other hand, compensated in part by broadening of the band gap due to quantum confinement effects.

Following the DFT calculations of the ZnO band structure [30], one has to expect the energetic levels near the upper edge of the valence band to be primarily formed from the 2p orbitals of oxygen. In a similar manner, energetic states near the lower edge of the conduction band originate from 4s levels of zinc. The valence and conduction band edges of the peroxide-synthesized materials are shifted toward lower energies with respect to those of the bulk disorder-free ZnO. The more negative energy of the upper edge of the valence band was observed also for samples with a characteristic particle size of 36 nm (i.e., outside the expected quantum confinement limit). The shift of the upper edge of the valence band can be attributed to the presence of overstoichiometric oxygen coordinating the zinc disordered in 2*a* sites. This oxygen acts as an n-type dopant, since its electron configuration approaches that of F. The position of the band edges does not change until the characteristic particle size drops below 10 nm. We can therefore take the electronic structure of the material with a particle size of 36 nm as an internal standard corresponding to a "bulk-disordered" ZnO. Further decrease of the particle size leads to a shift of the band edge positions corresponding to the theoretical model (i.e., the valence band edge shifts to more negative energies and the conduction band shifts to more positive energies). The shift of band edges is unequal for both valence and conduction bands, depending on the effective mass of the electron in the conduction band and of the hole in the valence band. In the case of ZnO, we ought to expect a larger effect of particle size on the conduction band edge due to a lower effective mass of the electron [28]. A nonlinear least squares (NLLS) fit of the experimental shift of band edge energies to Eq. 3 can be used to calculate the actual effective masses of electrons and holes as well as the relative dielectric constant of nanocrystalline ZnO (Fig. 10). Assuming that the behavior of the material is controlled by the particle size, one obtains a relative effective mass of electron and hole of 1.7 and 2.3,[1] respectively. These values are four to six times bigger than those predicted theoretically [28]. Assuming the control of the behavior by the size of the crystallographic coherent domain, one obtains a better agreement of experimental data with theory; the experimentally found values of electron and hole effective mass of 0.6 and 0.9, respectively, are only double of the theoretical prediction [28]. It suggests that the electronic structure of the

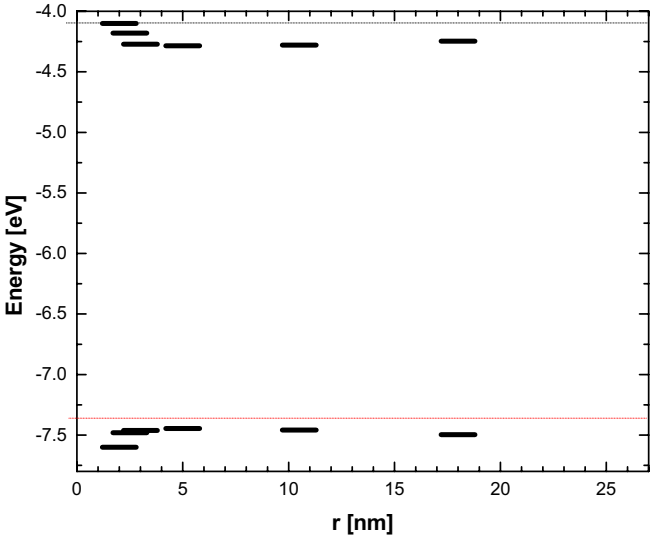

Fig. 9 Band edge energies as a function of particle radius. *Dotted lines* represent the band edge energies of bulk ZnO and are added for comparison

[1] Effective masses are related to the mass of electrons.

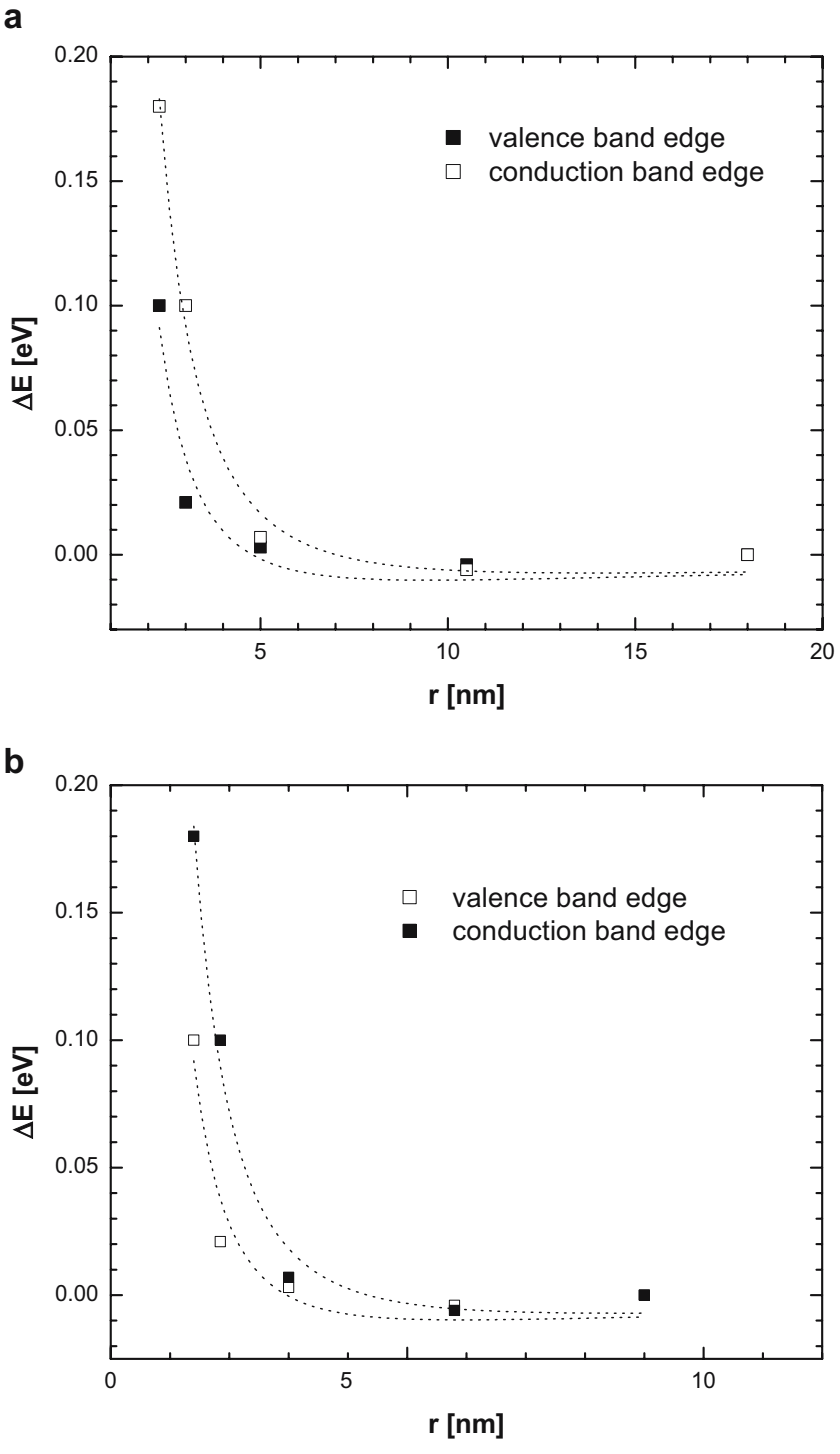

Fig. 10 Energy shift of the conduction band edge (*solid squares*) and of the valence band edge (*open squares*) as a function of particle radius (**a**) and coherent domain radius (**b**)

nanocrystalline material is controlled by coherent domain dimension rather than by particle size. The actual deviation of the electron and hole effective masses may be attributed to Zn disorder. The relative dielectric constant of the nanocrystalline ZnO obtained from the NLLS fit of the data was 9±3. This value is bigger than that predicted theoretically (3.7) [28]; however, it shows better agreement with the previously reported value (6± 2) [1b].

Conclusions

The thermal decomposition of zinc peroxide leads to the formation of nanocrystalline zinc oxide with a characteristic particle size between 5 and 40 nm. The particle size of the prepared material is proportional to the annealing temperature. Preparation of materials with particle sizes smaller than 10 nm requires reactions at lowered pressure.

Rietveld refinement of the powder diffraction patterns of prepared samples indicates that the zinc present in the materials is distributed between two types of sites of C_3v symmetry corresponding (in Wykoff notation) to sites of 2*a* and 2*b* type. The fraction of Zn in 2*a* position decreases with annealing temperature. The presence of Zn disorder affects the electronic structure of the prepared nanocrystalline zinc oxide. The upper edge of the valence band is shifted to lower energies, which can be attributed to oxygen atoms coordinating Zn in 2*a* positions. The band gap width determined from UV–Vis spectra is generally narrower than that of bulk disorder-free ZnO. A decrease of the particle size toward quantum confinement limit leads to a shift of band edge energies in accordance with theoretical predictions. The conduction band edge shift is more pronounced than that of the valence band edge as conforms with an expected lower effective mass of an electron (0.6) compared to that of a hole (0.9). The relative dielectric constant found for disordered ZnO (9±3) is significantly bigger than that predicted for ZnO theoretically; it shows better agreement with previously published experimental data [1b].

Acknowledgement This work was supported by the Academy of Sciences of the Czech Republic under contract T400400413.

References

1. (a) Grätzel M (2001) Nature 414:338; (b) Enright B, Fitzmaurice D (1996) J Phys Chem 100:1027
2. Bowker M, Hadden RA, Houghton H, Hyland JNK, Waugh KC (1988) J Catal 109:263
3. Lindsay R, Gutierrez-Sosa A, Thornton G, Ludviksson A, Parker S, Campbell GT (1999) Surf Sci 439:131
4. Huang MH, Mao S, Feick HN, Yan HQ, Wu YY, Kind H, Weber E, Russo R, Yang PD (2001) Science 292:1897
5. Cao H, Xu JY, Chang RPH (2000) Phys Rev Lett 84:5584
6. Aoki T, Hatanaka Y, Look DC (2000) Appl Phys Lett 76:3257
7. Heo YW, Norton DP, Tien LC, Kwon Y, Kang BS, Ren F, Pearton SJ, LaRoche JR (2004) Mater Sci Eng R 47:1
8. Rodriguez-Paez JE, Caballero AC, Villegas M, Moure C, Duran P, Fernandez JF (2001) J Eur Ceram Soc 21:925
9. Hoyer P, Eichberger R, Weller H (1993) Ber Bunsenges Phys Chem 97:630
10. Meulenkamp EA (1999) J Phys Chem B 103:7831
11. Asadov A, Gao W, Li Z, Lee J, Hodgson M (2005) This Solid Films 476:201
12. Lide DR (ed) (2004–2005) CRC handbook of chemistry and physics, 85th edn. CRC Press, Boca Raton, FL
13. Music S, Popovic S, Malikovic M, Dragcevic D (2002) J Alloys Compd 347:324
14. Stroyuk AL, Granchak VM, Korzhak AV, Kuchmii SYa (2004) J Photochem Photobiol A Chem 162:339
15. Yang Y, Chen H, Zhao B, Bao X (2004) J Cryst Growth 263:447
16. Lu HY, Chu ShY, Tan SS (2004) J Cryst Growth 269:385
17. Uekawa N, Mochizuki N, Kajiwara J, Mori F, Wu YJ, Kakegawa K (2003) Phys Chem Chem Phys 5:929
18. Ning G, Zhao X, Li J (2004) Opt Mater 27:1
19. Krumm S (1999) Comput Geosci 25:489
20. Acosta DR, Zironi EP, Montoya E, Estrada W (1996) Thin Solid Films 288:1
21. Puselj M, Ban Z, Morvaj J (1985) Documenta chemica Yugoslavica Croat Chem Acta 58:283
22. Schulz H, Thiemann KH (1979) Solid State Commun 32:783
23. Wagner CN, Aqua EN (1964) Adv X-ray Anal 7:46
24. Elliot RJ (1957) Phys Rev 108:1384
25. Syrbu NN, Tiginyanu IM, Zalamai VV, Ursaki VV, Rusu EV (2004) Physica B 353:111
26. van Dijken A, Meulenkamp EA, Vanmaekelbergh D, Meijerink A (2000) J Lumin 90:123
27. Fonoberov VA, Balandin AA (2004) Phys Rev B 70:195410
28. (a) Brus L (1986) J Phys Chem 90:2555; (b) Brus L (1984) J Chem Phys 80:4403
29. Halimi O, Boudine B, Sebais M, Chellouche A, Mouras R, Boudrioua A (2003) Mater Sci Eng C 23:1111
30. Yamamoto T, Katayamam-Yoshida H (2001) Physica B 155:302–303